Journal of Materials Chemistry A

Ultrahigh Capacity 2D Anode Materials for Lithium/Sodium-Ion Batteries: Entirely Planar B7P2 monolayer with Proper Pore Size and Distribution

Journal:	*Journal of Materials Chemistry A*
Manuscript ID	TA-ART-03-2020-002767.R1
Article Type:	Paper
Date Submitted by the Author:	15-Apr-2020
Complete List of Authors:	Zhu, Changyan; Northeast Normal University, Lin, Shiru; University of Puerto Rico, Rio Piedras Campus, Zhang, Min; Northeast Normal University, Department of Chemistry Li, Quan; Jilin University, College of Materials Science and Engineering Su, Zhong-Min; Northeast Normal University, Institute of Functional Material Chemistry, Faculty of Chemistry Chen, Zhongfang; University of Puerto Rico, Department of Chemistry

Ultrahigh Capacity 2D Anode Materials for Lithium/Sodium-Ion Batteries: Entirely Planar B_7P_2 monolayer with Proper Pore Size and Distribution

Changyan Zhu,[a] Shiru Lin,[b] Min Zhang,*[,a] Quan Li,[c]

Zhongmin Su,[a,d] Zhongfang Chen*[,b]

[a] Institute of Functional Material Chemistry, Faculty of Chemistry & National & Local United Engineering Laboratory for Power Battery, Northeast Normal University, Changchun 130024, China

[b] Department of Chemistry, Institute for Functional Nanomaterials, University of Puerto Rico Rio, Rio Piedras Campus, San Juan, PR 00931, USA

[c] State Key Laboratory of Superhard Materials, Key Laboratory of Automobile Materials of MOE, Department of Mate-rials Science, and Innovation Center for Computational Physics Method and Software, Jilin University, Changchun 130012, China

[d] School of Chemistry and Environmental Engineering, Changchun University of Science and Technology, Changchun 130024, China

Abstract

Lithium-ion batteries (LIBs) are widely used energy storage devices, and sodium-ion batteries (SIBs) are promising alternative to LIBs because sodium is of high abundance and low toxicity. However, a dominant obstacle for the advancement of LIBs and SIBs is the lack of high capacity anode materials, especially for SIBs. Here, we propose that three characteristics, namely appropriate pore size, proper porous distribution, and an entirely planar topology, can help achieve ultrahigh capacity 2D anode materials. Under such guidelines, we constructed the B_7P_2 monolayer, and investigated its potential as LIB/SIB anode materials by means of density functional theory (DFT) computations. Encouragingly, the B_7P_2 monolayer possesses all the essential properties for a high-capacity LIB/SIB anode: its high stability ensures the experimental feasibility for the synthesis, its metallicity does not change upon Li/Na adsorption and desorption, the Li/Na can well diffuse on the surface, and the open-circuit voltage is in a good range. Most importantly, B_7P_2 monolayer has a high storage capacity of 3117 mA h g^{-1} for both LIB and SIBs, this capacity value ranks among the highest for 2D SIB anode materials. This study offers us some good clues to design/discover other anode materials with ultrahigh capacities, and serves us another vivid example that (implicit and hidden) trends/rules in the literature can guide us design functional materials more efficiently.

1. Introduction

Rechargeable lithium-ion batteries (LIBs) are widely used in portable electronics and electric vehicles due to their merits of high energy densities, no memory effect, low self-discharge, and being environmentally benign.[1-4] Though both sodium-ion batteries (SIBs) and LIBs were studied as early as in the 1970s, LIBs have been the focus due to their much higher energy densities.[5-8] Sharing similar chemical properties of lithium, sodium possesses some superior characteristics for battery applications, such as lower toxicity and higher earth abundance. Hence, SIBs have been resurrected as appealing candidates for medium and large-scale stationary energy stor-age.[9-13] One of the largest obstacles restricting the SIBs' development and application is the limited anode storage capacity.[14-16] Therefore, it is indispensable to search ultrahigh-storage anode materials for rechargeable LIBs and SIBs, especially SIBs, to satisfy the ever-growing demands of high-density energy storage equipment in modern society.[17-20]

Two-dimensional (2D) materials are promising candidates for the next-generation LIB/SIB anode materials because of their high storage capacity, excellent electrical conductivity, and lower diffusion energy barrier.[21-24] The performance of many 2D materials as anode materials have been explored, such as graphene and its derivatives,[25-34] transition-metal dichalcogenides,[35-43] metal oxides,[44-53] and transition-metal carbides.[54-65] Especially, sodium storage capacities have been significantly improved in several 2D materials, even reaching the same capacities for lithium storage.[65-68]

Our careful analysis to the reported 2D anode materials revealed that some characteristics, such as appropriate pore size, proper distance between adsorption sites,

and an entirely planar topology, can greatly boost the Li/Na storage capacities. First, the appropriate pore size and the proper distance between adsorption sites are crucial for porous 2D materials since the most favorable adsorption sites for Li/Na atoms are typically over the pores, instead of on top of certain atoms, as observed in all the examples containing pores, such as the porous B_2S,[67] BP,[69] InP_3,[66] TiC_3,[64] and NiC_3[65] monolayers. Among them, the B_2S and BP monolayers, as an isoelectronic analogue of graphene, have larger interval between the adjacent adsorption sites than graphene (3.03 Å and 3.18 Å vs. 2.47 Å), and consequently smaller repulsive interactions between the adsorbed Li/Na atoms, which leads to the possibility to form a closely packed Li/Na layer on the B_2S and BP monolayers, and concomitant higher theoretical capacity for LIBs and SIBs.[67,69] Second, the entirely planar monolayer is beneficial to utilize more adsorption sites on the substrate. For example, the entirely planar NiC_3 monolayer (1698 mA h g^{-1})[65] possesses higher specific capacity than the puckered TiC_3 monolayer (1278 mA h g^{-1}).[64] Compared with the puckered monolayer, the flattened planar structure can better reduce the repulsive interactions among the Na atoms adsorbed on the reasonably well separately adsorption sites, thus promoting the Na loading amounts. Moreover, the experimentally available boron monolayer materials, including the puckered triangular-borophene,[70] the entirely planar striped borophene (β_{12}-borophene)[71] and χ_3-borophene[71], are all proposed to be high-performance anode materials for LIBs and SIBs. Among them, the entirely planar and porous β_{12}-borophene and χ_3-borophene were predicted to possess the same storage capacity (1984 mA h g^{-1} and 1240 mA h g^{-1}) for LIBs and SIBs.[68] However, the storage capacity of the

puckered triangular-borophene for Na (2341 mA h g^{-1}) is obvious lower than that for Li (3306 mA h g^{-1}),[72] and our computations showed that the entirely planar and porous β_{12}-borophene has a much higher Na storage capacity (3968 mA h g^{-1}) than the puckered triangular-borophene (2341 mA h g^{-1}) (Fig. S1 in Supporting Information). Therefore, the entirely planar topology is a hidden key characteristic to further boost the Na storage capacities.

With the above rationale in mind, we looked back to the reported candidates of 2D anode materials for LIBs/SIBs. One inspiring material is the experimentally available striped borophene (β_{12}-borophene),[71] which possess the highest single-layer storage capacity for SIBs. The high capacity of the boron nano-materials is attributed to the stronger binding interaction of B_7-unit (than B_6-unit) with Li/Na atom and the longer distance between adjacent potential adsorption sites. Though with the same pore size and the same entirely planar topology, χ_3-borophene has a lower Li/Na storage capacity than β_{12}-borophene,[68] which is relevant to its shortage of B_7-units. Therefore, introducing another element with bigger atomic radio but keeping B_7-units is able to tune the pore size and their distribution. What equally inspiring are the black phosphorene, blue phosphorene, and the BP monolayer, their superior capacities (865 mA h g^{-1} in black phosphorene[73] and 865 mA h g^{-1} in blue phosphorene[74] for SIBs, 1283 mA h g^{-1} in BP monolayer[69] for LIBs) strongly demonstrate the high potential of P element for anode materials of LIBs and SIBs. The exceptional Li/Na storage capacities of borophene and phosphorene prompted us to consider the B-P binary monolayers. Especially, a B_7P_2 binary monolayer, which can be constructed by

replacing some C_6-units in graphene by B_7-units and substituting the remaining C atoms by P atoms (symmetry P6/MMM), caught our great attention (Fig. 1a), since the larger radius of P (relative to that of B) can help separate the B_7-units, and the lone pair electron on P's p_z orbital is beneficial to stabilize the planar structure.

In this work, we systematically explored the potential of the B_7P_2 binary monolayer as LIB/SIB anode materials. This monolayer is of high stability and is confirmed to be the global minimum in the 2D space, thus rather feasible for experimental realization. The B_7P_2 monolayer is metallic, its intrinsic metallicity is well retained at different Li/Na concentrations, and has low Li/Na diffusion barriers and small average open-circuit voltages. Most excitingly, its capacity for both LIBs and SIBs reaches 3117 mA h g^{-1}, especially, its Na storage capacity is among the highest in 2D materials.[72] All these unique and exceptional characteristics make the B_7P_2 monolayer a promising 2D ultrahigh capacity anode material for LIBs and SIBs. We also believe that our proposed principles can be used to design even more such anode materials.

2. Computational methods

The B_7P_2 monolayer is confirmed to be the global minimum by the particle-swarm optimization (PSO) method within the evolutionary scheme as implemented in the CALYPSO code,[75] which is very effective to find the ground or metastable structures at a given chemical composition.[76-78] In our PSO simulation, the population size and the number of generations are both set to be 30. Unit cells containing 1, 2 and 4 formula

units (f.u.) are considered. The structure optimizations and electronic properties calculations are performed at the level of density functional theory (DFT) using the Vienna ab initio Simulation Package (VASP).[79] The Perdew-Burke-Ernzerhof (PBE) function with van der Waals (vdW) interaction proposed by Grimme (DFT-D2) is adopted.[80,81] The projector augmented-wave (PAW) pseudopotential is utilized to represent electron-ion interactions.[82,83] A vacuum distance of 30 Å along the *z* direction is used to avoid interactions between adjacent layers. The lane-wave cutoff energy of 600 eV is employed in all the computations. The convergence threshold is set as 10^{-6} eV in energy and 10^{-2} eV $Å^{-1}$ in force. The Monkhorst-Pack *k*-point mesh resolution in reciprocal space is $2\pi\times0.02$ $Å^{-1}$. The hybrid Heyd-Scuseria-Ernzerhof (HSE06) functional is used to obtain more accurate density of states (DOS) and band structure of the lowest-energy B_7P_2 monolayer.[84]

To evaluate the thermodynamic stability of the B_7P_2 monolayer, the cohesive energy (E_{coh}) defined as $E_{coh} = (7E_B + 2E_P - E_{B_7P_2})/9$ is calculated, where the E_B, E_P and $E_{B_7P_2}$ are the energies of the isolated B and P atoms and the B_7P_2 monolayer. To assess the kinetic stability, phonon dispersion of the B_7P_2 monolayer is computed using the finite displacement method as implanted in the PHONOPY program.[85] To evaluate its thermal stability, the ab initio molecular dynamics (AIMD) simulations using PBE functional and PAW pseudopotential are performed with 3×3 supercell at different temperatures. AIMD simulations in NVT ensemble lasts for 10 *ps* with a time step of 1.0 *fs*. The temperature is con-trolled by Nose-Hoover thermostat.[86]

To investigate the Li and Na diffusion energy barrier on the B_7P_2 monolayer, the climbing-image nudged elastic band (CI-NEB) method is used to search the minimum energy pathway between the given initial and final configurations.[87]

To evaluate if Li/Na atoms can be favorably adsorbed on the B_7P_2 monolayer to form $B_7P_2(Li/Na)_n$, we calculated both differential adsorption energy ($E_{ad\text{-}dif}$) and average adsorption energy ($E_{ad\text{-}ave}$) of Li/Na atom on the B_7P_2 monolayer. The differentia adsorption energy for $B_7P_2(Li/Na)_n$, defined as $E_{ad\text{-}dif} = E_{B_7P_2(Li/Na)_n} - E_{B_7P_2(Li/Na)_{n-1}} - E_{Li/Na}$, describes the energy released/needed when adding one more Li/Na atom on the $B_7P_2(Li/Na)_{n-1}$ structure. According to this definition, a negative $E_{ad\text{-}dif}$ value suggests favorable adsorption; however, a small positive value does not exclude the formation of the next atom adsorption since this step can be considered as an activation barrier to overcome when forming the structure with one more adsorbed atom. The average adsorption energy for $B_7P_2(Li/Na)_n$ is calculated by $E_{ad\text{-}ave} = (E_{B_7P_2(Li/Na)_n} - E_{B_7P_2} - nE_{Li/Na})/n$, and a negative value indicates the thermodynamic preference of forming a specific $B_7P_2(Li/Na)_n$ structure without metal atom clustering. Note that the volume and entropy changes during the adsorption process are neglected in our computations.

The average open-circuit voltage (OCV) is obtained by calculating the average voltage in the concentration range: $V_{ave} = -(E_{B_7P_2(Li/Na)_n} - E_{B_7P_2} - nE_{Li/Na})/ne$, in which $E_{B_7P_2(Li/Na)_n}$, $E_{B_7P_2}$, and $E_{Li/Na}$ are the energies of the B_7P_2 monolayer adsorbed with Li/Na atoms, the B_7P_2 monolayer in its global minimum, and a Li/Na atom in body-centered cubic (bcc) structure.[88]

The maximum capacity C is calculated by $C = 1000nF/(3600M)$ mA h g^{-1}, where n represents the maximum number of transferred electrons involved in the electrochemical process, F is the Faraday constant, and M is the mass of the B_7P_2 monolayer in g mol^{-1}.

3. Results and discussion

3.1. Structure, Stability and Electronic Properties of the B_7P_2 Monolayer - the Global Minimum in 2D Space

Inspired by the obvious distinction between graphene and borophene as anode materials, we identified an eligible B_7P_2 monolayer satisfying the proposed criteria, which is confirmed to be the global minima through a comprehensive PSO search combined with first-principles calculations. The unit cell of B_7P_2 monolayer consists of seven B atoms and two P atoms in the same plane with the optimized lattice constants of $a = b = 6.12$ Å (Fig. 1a). In the B_7P_2 monolayer, one central B atom binds with the six neighboring B atoms to form one B_7-unit. The B-B distances in these B_7-units (1.70 Å) are comparable to those in β_{12}-borophene (1.70 Å), which also consists of the entirely planar B_7-units. Meanwhile, each P atom binds with three B_7-units, and each B_7-unit is connected by six P atoms, forming a hexagonal B_4P_2-unit with the pore diameter of 3.53 Å and B-P distances of 1.84 Å. Note that the lattice parameters and the pore diameter of the B_4P_2-unit are both longer than those of graphene and borophenes (for the lattice parameters of graphene and borophenes, see Table S1 of Supporting Information), which is beneficial to reduce the repulsive interactions among

adsorbed Li/Na atoms according to our hypothesis, and is expected to help improve the Li/Na storage capacity.

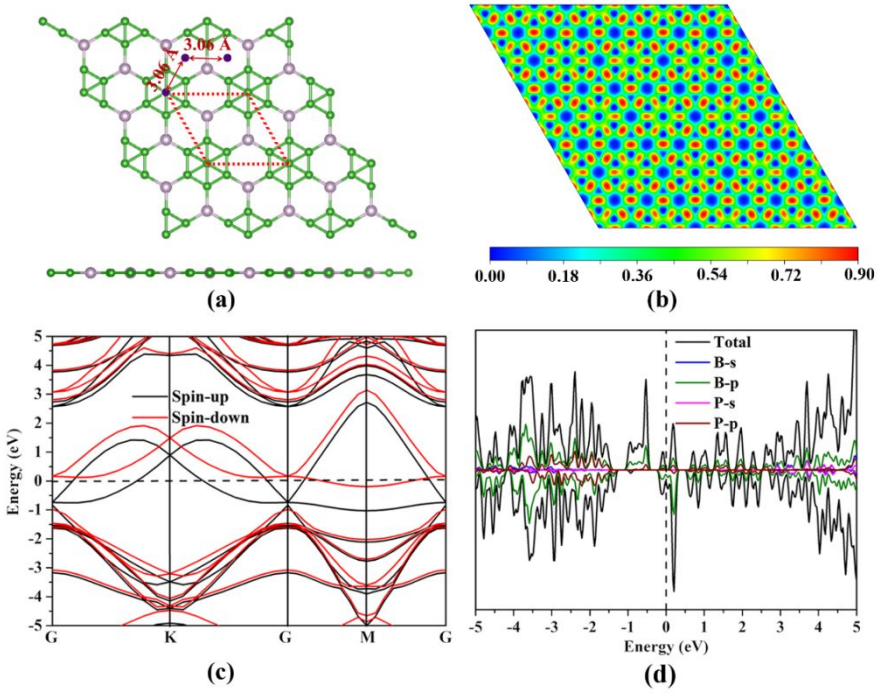

Fig. 1 (a) Optimized global minimum structure of B_7P_2 monolayer. The red dashed lines indicate its primitive cell, (b) Electron localization function (ELF) map sliced in (001) direction of B_7P_2 monolayer, (c) Electronic band structure of B_7P_2 monolayer using HSE06 functional, (d) Projected densities of states (PDOS) of B_7P_2 monolayer using HSE06 functional. The Fermi lev-el is set to zero.

To understand the bonding nature in the B_7P_2 monolayer, we plotted its electron localization function (ELF)[89] map in the (001) direction (Fig. 1b). Note that the values of 1.0 and 0.5 represent the perfect localization and the free electron-gas, while the value near zero denotes a low electron density area. For the B_7P_2 monolayer, the electron density of 0.9 around P atoms along three directions in the (001) direction

suggests the significant B-P covalent bonding. On the other hand, the other three π electrons in the B_7-unit and the two electrons in p_z orbital of the P atoms are delocalized in the whole monolayer framework with the electron density of around 0.25.

To understand the charge distribution of the B_7P_2 monolayer, we analyzed the deformation electronic density (DED). The deformation electronic density is defined as the difference between the total electronic density and the electronic density of the isolated atoms. The remarkable electron transfer occurs from the B_7-unit to the P atoms (Fig. S2), which can be confirmed by the Bader charge (-0.73|e| on each P atom) and Hirshfeld charge (-0.14|e| on each P atom) analyses. The covalent B-P σ bonds and delocalized π electrons in the whole framework guarantee its superior stability, and the unoccupied π orbitals in the B_7-units are expected to benefit the electron diffusion upon Li/Na adsorption, as confirmed by our computations in Section 3.2.

Our computations also found that the B_7P_2 monolayer has a spin-polarized ferromagnetic ground state, which is 12.6 meV per unit cell lower in energy than the nonmagnetic state. The spin density distribution (Fig. S3) shows that the spin-polarized electrons are mainly localized on the peripheral six B atoms of the B_7-unit. The B_7P_2 monolayer is metallic, and the high electron density near the Fermi level is well revealed. The conducting nature is mainly originated from the p orbitals of B atoms (Fig. 1c and Fig. 1d). The outstanding electronic conductivity is also beneficial for its application as LIB/SIB anode materials.

The B_7P_2 monolayer is of superior thermodynamic, kinetic, thermal, and mechanical stabilities. The calculated cohesive energy of B_7P_2 monolayer (5.49

eV/atom) is comparable to those of the experimentally available borophenes, including triangular-borophene (5.90 eV/atom),[70] β_{12}-borophene (5.95 eV/atom),[71] and χ_3-borophene (5.96 eV/atom),[71] and it is much higher than that of the phosphorene (3.48 eV/atom)[90] computed at the same theoretical level. Such a high cohesive energy suggests that B_7P_2 monolayer is a strongly bonded network and of good thermodynamic stability. This monolayer is also kinetically stable, as indicated by the absence of any imaginary frequency in the phonon dispersion curve in the whole Brillouin zone (Fig. S4). Moreover, B_7P_2 monolayer can well maintain its original configuration with the B_7-units and the hexagonal B_4P_2-units up to 2000 K at the end of 10 *ps* MD simulations (the final snapshots of B_7P_2 monolayer structures at the temperatures of 500 K, 1000 K, 1500 K and 2000 K are given in Fig. S5), and the distorted structures after MD simulations can restore the entirely planar structure upon full structural relaxation, indicating its high thermal stability. Furthermore, we evaluated the mechanical stability of the B_7P_2 monolayer. The calculated elastic constants of the B_7P_2 monolayer are C_{11}=175.24 N m^{-1}, C_{22}=173.37 N m^{-1}, C_{12} = C_{21} =45.15 N m^{-1} and C_{66} =63.79 N m^{-1}, which satisfy the mechanical stability criteria: $C_{11}C_{22}$-C_{12}^2 > 0, C_{66} > 0. Thus, the B_7P_2 monolayer is mechanically stable. Though the in-plane Young's modulus (Y_a and Y_b) along *a* and *b* direction of the B_7P_2 monolayer (163.48 N m^{-1} and 161.74 N m^{-1}, respectively) are less than those of graphene (341.60 N m^{-1}),[91] they are higher than the corresponding values of the experimentally available MoS_2 monolayer (126 N m^{-1})[92] and Cu_2Si monolayer (84.51 N m^{-1}),[93] suggesting the B_7P_2 monolayer possesses promising mechanical application.

Finally, we examined the interlayer strength and stacking pattern when B_7P_2 monolayers are stacked together. Among the three considered bilayer stacking patterns (Fig. S6), the complete overlap (AA) stacking bilayer is energetically most favorable. Its computed interlayer energy (80 meV/atom at the interlayer distance of 2.85 Å) is even lower than the corresponding value (141 meV/atom at the distance of 3.08 Å) in the graphene bilayer.[94] Moreover, there is no obvious electron distribution between the upper-layer and lower-layer. These data indicate that B_7P_2 is inclined to be a monolayer, instead of stacking together to form multi-layers.

3.2. Li/Na Adsorption and Adatom Diffusion on the B_7P_2 Monolayer

To explore the potential of B_7P_2 monolayer as anode materials for rechargeable LIBs and SIBs, first we investigated the single Li/Na atom adsorption and diffusion on the B_7P_2 monolayer. The 2×2 supercell is used for the B_7P_2 monolayer, and three possible adsorption sites on B_7P_2 monolayer, namely S1, S2 and S3 (Fig. 2a) are considered due to its high symmetry (P6/MMM). S1 locates over the center of the B_4P_2-unit, or at the pore center; S2 is over the center of the B_7-unit; S3 is over the top site of P atom.

The calculated Li/Na adsorption energies (E_{ad}) on all these three adsorption sites are negative, suggesting that the process of single Li/Na atom adsorption on the B_7P_2 monolayer is exothermic. Note that the energetically most favorable adsorption site for a single Li/Na atom is the S1 site above the pore center, with E_{ad} values of -1.54 and -1.41 eV for Li and Na, respectively. The preferential adsorption on the S1 site strongly supports our hypothesis that the existence of proper pores would enhance the Li/Na

adsorption. The S2 site is the second favorable position (E_{ad}: -1.28 eV for Li, -1.20 eV for Na), followed by the S3 site (E_{ad}: -0.94 eV for Li, -1.09 eV for Na). The short distance between S1 and S3 sites (1.77 Å) suggests that the adsorption on the S3 site is very likely unfavorable once the energetically most favorable S1 site is occupied.

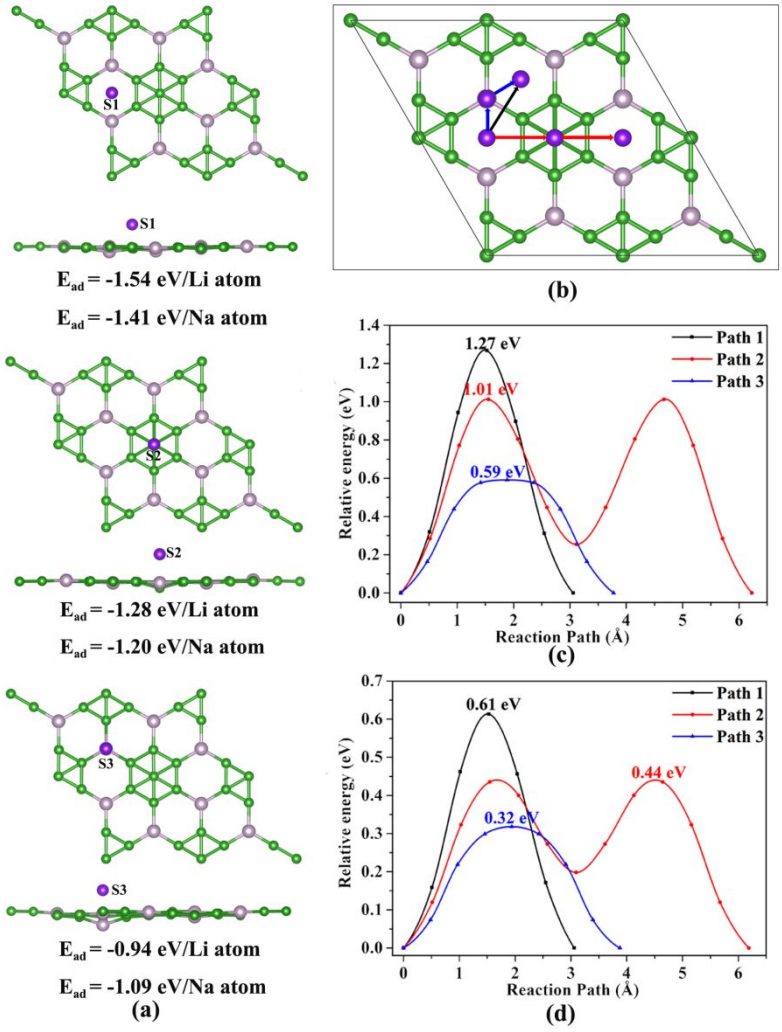

Fig. 2 (a) Optimized structures and corresponding adsorption energy (E_{ad}) of single Li/Na atom on three adsorption sites of the B_7P_2 monolayer, respectively, (b) Possible Li/Na diffusion pathways on the B_7P_2 monolayer, Paths 1, 2, and 3 are marked by black, red and blue. (c) Li and (d) Na diffusion energy barriers on the B_7P_2 monolayer.

After adsorption, significant charge transfer from the adsorbed Li/Na atom to the B_7P_2 monolayer occurs, as indicated by the ELF map of the Li/Na adsorbed B_7P_2 monolayer (Fig. S7), and the calculated Bader charge and Hirshfeld charge of the single Li/Na atoms on the monolayer (Table S2). The electron transfer (0.8|e| according to Bader charge analysis) is comparable to that on borophenes,[68,95,96] which demonstrates strong ionic interactions between the adsorbed Li/Na atom and the substrate B_7P_2 monolayer.

To theoretically evaluate the charge/discharge rate of our newly proposed anode material, we investigated the diffusion pathways and the corresponding barriers of a single Li/Na ion on the B_7P_2 monolayer among different adsorption sites. In our computations, the energetically most preferred adsorption site, namely S1, is defined as the starting and the ending position for the Li/Na diffusion. Accordingly, there are three different diffusion pathways between two nearest neighboring adsorption sites (Fig. 2b): (i) Path 1, in which the adsorbed Li/Na diffuses directly from one S1 site to another nearest S1 site; (ii) Path 2, in which the adsorbed Li/Na moves to another S1 site passing through its nearest S2 site; and (iii) Path 3, in which the adsorbed Li/Na transfers to another S1 site passing through its nearest S3 site. According to the calculated Li/Na diffusion barriers (Fig. 2c and Fig. 2d), Path 3 is the most optimal pathway for both Li and Na diffusion, the Li/Na diffusion barriers (0.59 and 0.32 eV for Li and Na, respectively) are slightly lower than those on β_{12}-borophene and χ_3-borophene,[67] and the corresponding Li/Na diffusion lengths are 3.77 Å and 3.88 Å, respectively. Notably, the S3 site is the highest energy point of diffusion pathway along path 3, which indicates

that the adsorbed Li/Na cations can't accommodate on this adsorption sites in practical applications. Though with the shortest possible distance, diffusion along Path1 has the highest barriers (1.27 and 0.68 eV for Li and Na, respectively).

3.3. Maximum Storage Capacity and Open-circuit Voltage

We evaluated the maximum Li/Na storage capacity on the B_7P_2 monolayer through gradient increment strategy by considering 16 different concentrations ($B_7P_2(Li/Na)_n$, n=1-16). The most stable structures of the maximum Li/Na concentration, i.e., with the stoichiometry of $B_7P_2(Li/Na)_{16}$, are presented in Fig. 3(b) and Fig. 3(c), while those at lower L/Na concentrations are given in Fig. S8 and Fig. S9. The entirely planar structure of the B_7P_2 monolayer is somewhat puckered once the adsorption site S2 is occupied by the Li/Na atom. Moreover, when the Li/Na atoms are adsorbed on the substrate, the lattice constants of the B_7P_2 monolayer are slightly changed (up to 1.8%, Table S5). However, the slightly puckered structures and the lattice constants can quickly recover to the initial planar topography when the Li/Na atoms are removed from the B_7P_2 monolayer.

We calculated both the differential adsorption energy ($E_{ad\text{-}dif}$) and average adsorption energy ($E_{ad\text{-}ave}$) values at different lithiation/sodiation levels, as presented in Fig. 3(a) and Table S6. In general, the differential adsorption energy and average adsorption energy feature the same trend: both fluctuate and approach to zero when increasing the number of adsorbed Li/Na atoms. The calculated $E_{ad\text{-}ave}$ values are all negative and lower than the $E_{ad\text{-}diff}$ values, and only a few $E_{ad\text{-}diff}$ are slightly positive

(the maximum values are +0.25 eV for $B_7P_2Li_{12}$ and +0.20 eV for $B_7P_2Na_{15}$). At the highest concentration $B_7P_2(Li/Na)_{16}$, the calculated average adsorption energies are -0.28 eV/Li atom and -0.24 eV/Na atom, respectively, suggesting that the lithiated/sodiated monolayer does not suffer the metal clustering problem, in other words, the Li/Na atoms prefer being adsorbed separately on the B_7P_2 monolayer even at such a high Li/Na ratio. Thus, we expect that the maximum storage capacity can reach 3117 mA h g^{-1} with the stoichiometry of $B_7P_2(Li/Na)_{16}$.

Is the highly lithiated/sodiated B_7P_2 monolayer thermally stable? To address this question, we performed AIMD simulations of $B_7P_2Li_{16}$ and $B_7P_2Na_{16}$ with a 3×3 supercell at the temperatures of 300 K. Encouragingly, the adsorbed Li/Na atoms are well attached to the B_7P_2 monolayer after 10 *ps* simulations (Fig. S10), and the slight puckered B_7P_2 $(Li/Na)_{16}$ at the end of MD simulations can quickly recover to the initial planar topography when the Li/Na atoms are removed from B_7P_2 monolayer. Thus, the B_7P_2 monolayer is structurally stable even after high lithiation/sodiation, which is beneficial for recharged LIBs and SIBs.

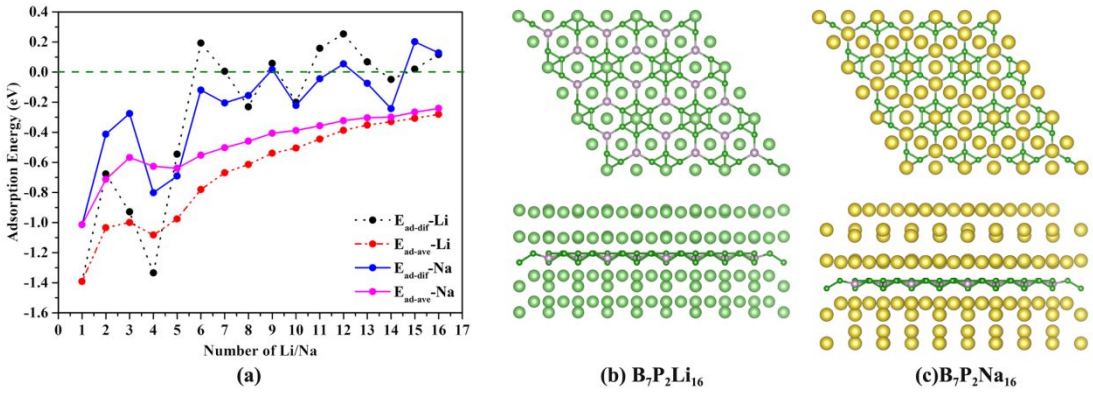

Fig. 3 (a) Differential adsorption energy ($E_{ad\text{-}dif}$) and average adsorption energy ($E_{ad\text{-}ave}$) of Li/Na atoms on the B_7P_2 monolayer. Top and side views of the most stable structure with the maximum (b) Li and (c) Na concentration on the B_7P_2 monolayer.

Notably, the maximum theoretical storage capacity of the B_7P_2 monolayer (corresponding to B_7P_2 $(Li/Na)_{16}$) is 3117 mA h g^{-1}, which is roughly comparable with the triangular-borophene for Li, and reaches a new record for Na among the reported 2D materials (372 mA h g^{-1} of graphite for Li,[29] 1498 mA h g^{-1} of B_2S monolayer for Li/Na,[67] 1283 mA h g^{-1} of BP monolayer for Li,[69] 3306 mA h g^{-1} of triangular-borophene for Li,[72] 2341 mA h g^{-1} of triangular-borophene for Na,[72] 1984 mA h g^{-1} of β_{12}-borophene for Li/Na,[68] 1240 mA h g^{-1} of χ_3-borophene for Li/Na,[68] 1278 mA h g^{-1} of TiC_3 monolayer for Na,[64] 1698 mA h g^{-1} of NiC_3 monolayer for Li/Na[65]). Such high storage capacities for Li and Na, especially Na, further validate our hypothesis that the latent characteristics, namely appropriate pore size, proper distance between adsorption sites, and an entirely planar topology of 2D anode materials, can greatly boost the Li/Na storage capacities.

In addition, the inherent metallicity of the B_7P_2 monolayer is well reserved at different Li/Na concentrations (Fig. S11 and Fig.S12), which is important for charge-discharge cycle. The calculated $B_7P_2(Li/Na)_n$ (n=1-16) are all metallic, expect $B_7P_2Li_5$ and $B_7P_2Na_5$ with small band gaps (0.43 eV and 0.09 eV, respectively). In comparison, the recently predicted anode materials for Na-ion batteries, P_3C monolayer, has a band gap of 0.77 eV upon sodiation to P_3CNa.[97]

To understand the origin of the high Li/Na storage capacities and the multi-layer adsorption behavior, we compared the ELF map sliced in (100) direction of the B_7P_2 monolayer with two representative Li/Na adsorption concentrations, i.e., $B_7P_2(Li/Na)_8$ with one layer of Li/Na atoms, and $B_7P_2(Li/Na)_{16}$ with two layers of Li/Na atoms (Fig. 4). Clearly, more electrons are transferred from the inner layer to the outer layer. Moreover, the dispersive electrons are well spread out in the metal layers, forming a negative electron cloud, which can effectively decrease the repulsion interactions among the adsorbed Li/Na atoms and stabilize the outer-layer Li/Na atoms.[98,99] Similar phenomenon has been observed for the multi-layer Na atom adsorption in the MoN_2 monolayer.[100]

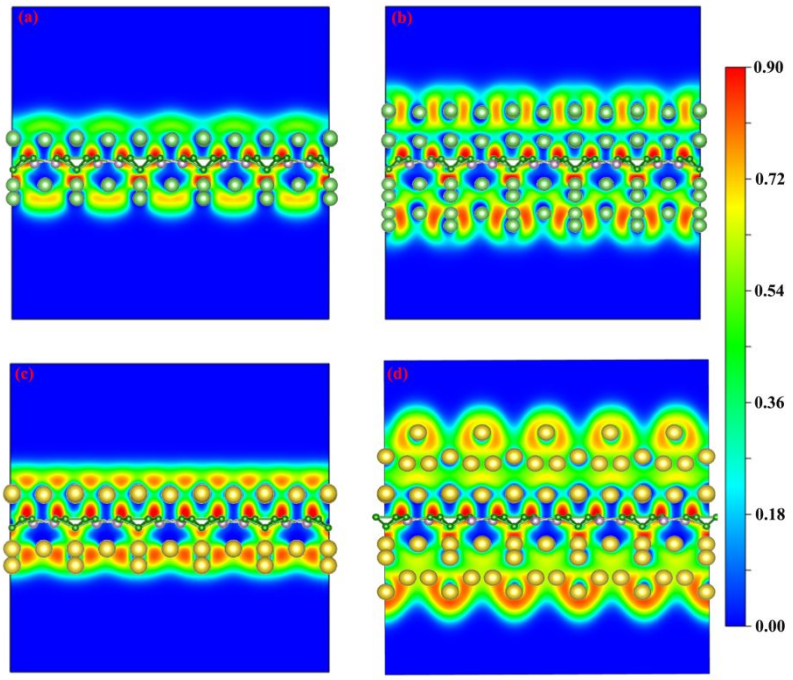

Fig. 4 ELF map sliced in (100) direction of B_7P_2 monolayer with (a) one layer of Li atoms ($B_7P_2Li_8$), (b) two layers of Li atoms ($B_7P_2Li_{16}$), (c) one layer of Na atoms ($B_7P_2Na_8$), (d) two layers of Na atoms ($B_7P_2Na_{16}$).

The theoretical open-circuit voltage (OCV) values, as another important parameter to evaluate the performance of the anode materials, are in the range of 0.24-1.39 V at the 16 different Li/Na concentrations examined here (Table S3). Such OCV values are also beneficial for our predicted anode material, since it will result in a larger cathode-anode voltage difference, thus a higher cell voltage.

4. Conclusions

Our analysis into the reported 2D anode materials revealed that some characteristics, namely appropriate pore size, proper distance between adsorption sites, and an entirely planar topology, could boost the Li/Na storage capacity, thus help

achieve ultrahigh capacity anode materials for LIBs and SIBs. Guided by these insights and encouraged by recent discoveries of using borophene and phosphorene as high-performance LIB/SIB anode materials, we constructed the B_7P_2 monolayer with similar topologies as borophene by combining the B_7-units in borophene and the P element with a larger atomic radius. Our computations showed that the proposed structure is the global minimum in the 2D space and possesses the essential properties as a promising ultrahigh capacity LIB/SIB anode material: it has superior thermodynamic, kinetic, thermal and mechanical stabilities, preserves its intrinsic metallicity at upon Li/Na adsorption and desorption, and has a high Li/Na mobility and relatively small average open-circuit voltages. Encouragingly, its capacity (3117 mA h g^{-1}) is eight times higher than the commercial graphite for LIBs, and among the highest among 2D SIB anode materials.

We strongly encourage further studies into the purely planar 2D materials containing high abundance of reasonably well separately pores with proper sizes, which are promising candidates for ultrahigh capacity LIB/SIB anode materials, and believe that revealing the trends/rules in the vast literature, which may be implicit or hidden, will greatly accelerate our materials discovery process.

Conflicts of interest

There are no conflicts to declare.

Acknowledgements

The work is financially supported in China by National Natural Science Foundation of China (21673036 and 21771035) and in USA by NSF Center for the Advancement of Wearable Technologies (Grant 1849243). Most computations were carried out on TianHe-2 at LvLiang Cloud Computing Center of China. We acknowledge the support of the computational resources from Institute of Theoretical Chemistry, Jilin University. In addition, we are grateful to the MatCloud (http://matcloud.cnic.cn) for discussion and computational support.

Electronic Supplementary Information

Maximum Na capacity of the β_{12}-borophene; validation of our computational methods; charge analysis; OCV of $B_7P_2(Li/Na)_n$; structural parameters, deformation electronic density, spin-polarized, snapshots of the B_7P_2 monolayer equilibrium structures at the end of AIMD simulations, details about the B_7P_2 bilayer, ELF map of the B_7P_2 monolayer after adsorbing a single Li/Na atom, electronic band structure of the B_7P_2 monolayer with different Li/Na adsorption ratios, snapshots of $B_7P_2(Li/Na)_{16}$ at the end of AIMD simulations, most stable structures of $B_7P_2(Li/Na)_n$.

References

1 D. P. Dubal, O. Ayyad, V. Ruiz and P. Gomez-Romero, *Chem. Soc. Rev.*, 2015, **44**, 1777-1790.

2 J. W. Choi and D. Aurbach, *Nat. Rev. Mater.*, 2016, **1**, 16013.

3 S. Hy, H. Liu, M. Zhang, D. Qian, B. J. Hwang and Y. S. Meng, *Energy Environ.*

Sci., 2016, **9**, 1931-1954.

4 M. Li, J. Lu, Z. Chen and K. Amine, *Adv. Mater.*, 2018, **30**, 1800561.

5 N. Oyama, T. Tatsuma, T. Sato and T. Sotomura, *Nature*, 1995, **373**, 598.

6 Y. Idota, T. Kubota, A. Matsufuji, Y. Maekawa and T. Miyasaka, *Science*, 1997, **276**, 1395-1397.

7 M. Armand and J. M. Tarascon, *Nature*, 2008, **451**, 652.

8 P. Simon, Y. Gogotsi and B. Dunn, *Science*, 2014, **343**, 1210-1211.

9 S. W. Kim, D. H. Seo, X. Ma, G. Ceder and K. Kang, *Adv. Energy Mater.*, 2012, **2**, 710-712.

10 V. Palomares, P. Serras, I. Villaluenga, K. B. Hueso, J. Carretero-González and T. Rojo, *Energy Environ. Sci.*, 2012, **5**, 5884-5901.

11 M. D. Slater, D. Kim, E. Lee and C. S. Johnson, *Adv. Funct. Mater.*, 2013, **23**, 947-958.

12 Y. Liang, W. H. Lai, Z. Miao and S. L. Chou, *Small*, 2018, **14**, 1702514.

13 C. Delmas, *Adv. Energy Mater.*, 2018, **8**, 1703137.

14 N. Yabuuchi, K. Kubota, M. Dahbi and S. Komaba, *Chem. Rev.*, 2014, **114**, 11636-11682.

15 D. Kundu, E. Talaie, V. Duffort and L. F. Nazar, *Angew. Chem. Int. Ed.*, 2015, **54**, 3431-3448.

16 P. K. Nayak, L. Yang, W. Brehm and P. Adelhelm, *Angew. Chem. Int. Ed.*, 2018, **57**, 102-120.

17 M. Winter and R. J. Brodd, *Chem. Rev.*, 2004, **104**, 4245-4269.

18 V. Etacheri, R. Marom, R. Elazari, G. Salitra and D. Aurbach, *Energy Environ. Sci.*, 2011, **4**, 3243-3262.

19 J. Sun, H. W. Lee, M. Pasta, H. Yuan, G. Zheng, Y. Sun, Y. Li and Y. Cui, *Nat. Nanotechnol.*, 2015, **10**, 980-986.

20 M. Lao, Y. Zhang, W. Luo, Q. Yan, W. Sun and S. X. Dou, *Adv. Mater.*, 2017, **29**, 1700622.

21 H. Cui, Y. Guo, W. Ma and Z Zhou, *ChemSusChem*, 2020, **13**, 1155-1171.

22 Y. Jing, Z. Zhou, C. R. Cabrera and Z. Chen, *J. Mater. Chem. A*, 2014, **2**, 12104-12122.

23 A. Gupta, T. Sakthivel and S. Seal, *Prog. Mater Sci.*, 2015, **73**, 44-126.

24 L. Shi and T. Zhao, *J. Mater. Chem. A*, 2017, **5**, 3735-3758.

25 D. Wu, Y. Li and Z. Zhou, *Theor. Chem. Acc.*, 2011, **130**, 209-213.

26 A. L. M. Reddy, A. Srivastava, S. R. Gowda, H. Gullapalli, M. Dubey and P. M. Ajayan, *ACS Nano*, 2010, **4**, 6337-6342.

27 X. Fan, W. Zheng and J. L. Kuo, *ACS Appl. Mater. Interfaces*, 2012, **4**, 2432-2438.

28 V. Chabot, D. Higgins, A. Yu, X. Xiao and Z. Chen, *J. Energy Environ. Sci.*, 2014, **7**, 1564-1596.

29 X. Wang, Q. Weng, X. Liu, X. Wang, D. M. Tang, W. Tian, C. Zhang, W. Yi, D. Liu and Y. Bando, *Nano Lett.*, 2014, **14**, 1164-1171.

30 O. I. Malyi, K. Sopiha, V. V. Kulish, T. L. Tan, S. Manzhos and C. Persson, *Appl. Surf. Sci.*, 2015, **333**, 235-243.

31 B. Luo and L. Zhi, *Energy Environ. Sci.*, 2015, **8**, 456-477.

32 M. Zhou, X. Li, B. Wang, Y. Zhang, J. Ning, Z. Xiao, X. Zhang, Y. Chang and L. Zhi, *Nano Lett.*, 2015, **15**, 6222-6228.

33 L. Zhou, Z. Hou, B. Gao and T. Frauenheim, *J. Mater. Chem. A*, 2016, **4**, 13407-13413.

34 J. Yang, X. Zhou, D. Wu, X. Zhao and Z. Zhou, *Adv. Mater.*, 2017, **29**, 1604108.

35 Y. Li, D. Wu, Z. Zhou, C. R. Cabrera and Z. Chen, *J. Phys. Chem. Lett.*, 2012, **3**, 2221-2227.

36 M. Pumera, Z. Sofer and A. Ambrosi, *J. Mater. Chem. A*, 2014, **2**, 8981-8987.

37 T. Stephenson, Z. Li, B. Olsen and D. Mitlin, *Energy Environ. Sci.*, 2014, **7**, 209-231.

38 R. Bhandavat, L. David and G. Singh, *J. Phys. Chem. Lett.*, 2012, **3**, 1523-1530.

39 B. Qu, C. Ma, G. Ji, C. Xu, J. Xu, Y. S. Meng, T. Wang and J. Y. Lee, *Adv. Mater.*, 2014, **26**, 3854-3859.

40 H. Jiang, D. Ren, H. Wang, Y. Hu, S. Guo, H. Yuan, P. Hu, L. Zhang and C. Li, *Adv. Mater.*, 2015, **27**, 3687-3695.

41 E. Yang, H. Ji and Y. Jung, *J. Phys. Chem. C*, 2015, **119**, 26374-26380.

42 X.Wang, Q. Weng, Y. Yang, Y. Bando and D. Golberg, *Chem. Soc. Rev.*, 2016, **45**, 4042-4073.

43 D. B. Putungan, S. H. Lin and J. L. Kuo, *ACS Appl. Mater. Interfaces*, 2016, **8**, 18754-18762.

44 C. Arrouvel, S. C. Parker and M. S. Islam, *Chem. Mater.*, 2009, **21**, 4778-4783.

45 J. Procházka, L. Kavan, M. Zukalová, O. Frank, M. Kalbáč, A. T. Zukal, M.

Klementová, D. Carbone and M. Graetzel, *Chem. Mater.*, 2009, **21**, 1457-1464.

46 T. Beuvier, M. Richard-Plouet, M. Mancini-Le Granvalet, T. Brousse, O. Crosnier and L. Brohan, *Inorg. Chem.*, 2010, **49**, 8457-8464.

47 A. S. Dalton, A. A. Belak and A. Van der Ven, *Chem. Mater.*, 2012, **24**, 1568-1574.

48 A. G. Dylla, P. Xiao, G. Henkelman and K. J. Stevenson, *J. Phys. Chem. Lett.*, 2012, **3**, 2015-2019.

49 S. Liu, H. Jia, L. Han, J. Wang, P. Gao, D. Xu, J. Yang and S. Che, *Adv. Mater.*, 2012, **24**, 3201-3204.

50 A. G. Dylla, G. Henkelman and K. J. Stevenson, *Acc. Chem. Res.*, 2013, **46**, 1104-1112.

51 H. Sugaya, K. Fukuda, M. Morita, H. Murayama, E. Matsubara, T. Kume and Y. Uchimoto, *Chem. Lett.*, 2015, **44**, 1595-1597.

52 J. Ni, Y. Zhao, L. Li and L. Mai, *Nano Energy*, 2015, **11**, 129-135.

53 M. Liu, C. Yan and Y. Zhang, *Sci. Rep.*, 2015, 5, 8326.

54 Q. Tang, Z. Zhou and P. Shen, *J. Am. Chem. Soc.*, 2012, 134, 16909-16916.

55 M. Naguib, J. Halim, J. Lu, K. M. Cook, L. Hultman, Y. Gogotsi and M. W. Barsoum, *J. Am. Chem. Soc.*, 2013, **135**, 15966-15969.

56 Y. Xie, M. Naguib, V. N. Mochalin, M. W. Barsoum, Y. Gogotsi, X. Yu, K. W. Nam, X. Q. Yang, A. I. Kolesnikov and P. R. Kent, *J. Am. Chem. Soc.*, 2014, **136**, 6385-6394.

57 D. Sun, Q. Hu, J. Chen, X. Zhang, L. Wang, Q. Wu and A. Zhou, *ACS Appl. Mater.*

Interfaces, 2015, **8**, 74-81.

58 E. Yang, H. Ji, J. Kim, H. Kim and Y. Jung, *Phys. Chem. Chem. Phys.*, 2015, **17**, 5000-5005.

59 Q. Sun, Y. Dai, Y. Ma, T. Jing, W. Wei and B. Huang, *J. Phys. Chem. Lett.*, 2016, **7**, 937-943.

60 J. Halim, S. Kota, M. R. Lukatskaya, M. Naguib, M. Q. Zhao, E. J. Moon, J. Pitock, J. Nanda, S. J. May and Y. Gogotsi, *Adv. Funct. Mater.*, 2016, **26**, 3118-3127.

61 M. Ashton, R. G. Hennig and S. B. Sinnott, *Appl. Phys. Lett.*, 2016, **108**, 023901.

62 Z Xu, X. Lv, J. Chen, L. Jiang, Y. Lai and J. Li, *Phys. Chem. Chem. Phys.*, 2017, **19**, 7807-7819.

63 T. Yu, S. Zhang, F. Li, Z. Zhao, L. Liu, H. Xu and G. Yang, *J. Mater. Chem. A*, 2017, **5**, 18698-18706.

64 T. Yu, Z. Zhao, L. Liu, S. Zhang, H. Xu and G. Yang, *J. Am. Chem. Soc.*, 2018, **140**, 5962-5968.

65 C. Zhu, X. Qu, M. Zhang, J. Wang, Q. Li, Y. Geng, Y. Ma and Z. Su, *J. Mater. Chem. A*, 2019, **7**, 13356-13363.

66 J. Liu, C. S. Liu, X. J. Ye and X. H. Yan, *J. Mater. Chem. A*, 2018, **6**, 3634-3641.

67 P. Li, Z. Li and J. Yang, *J. Phys. Chem. Lett.*, 2018, **9**, 4852-4856.

68 X. Zhang, J. Hu, Y. Cheng, H. Y. Yang, Y. Yao and S. A. Yang, *Nanoscale*, 2016, **8**, 15340-15347.

69 H. Jiang, W. Shyy, M. Liu, L. Wei, M. Wu and T. Zhao, *J. Mater. Chem. A*, 2017, **5**, 672-679.

70 A. J. Mannix, X. F. Zhou, B. Kiraly, J. D. Wood, D. Alducin, B. D. Myers, X. Liu, B. L. Fisher, U. Santiago and J. R. Guest, *Science*, 2015, **350**, 1513-1516.

71 B. Feng, J. Zhang, Q. Zhong, W. Li, S. Li, H. Li, P. Cheng, S. Meng, L. Chen and K. Wu, *Nat. Chem.*, 2016, **8**, 563.

72 D. W. Rao, L. Y. Zhang, Z. S. Meng, X. R. Zhang, Y. H. Yang, G. J. Qiao, X. Q. Shen, H. Xia, J. H. Liu and R. F. Lu, *J. Mater. Chem. A*, 2017, **5**, 2328-2338.

73 V. Kulish, O. Malyi, C. Persson and P. Wu, *Phys. Chem. Chem. Phys.*, 2015, **17**, 13921-13928.

74 S. Mukherjee, L. Kavalsky and C. Singh, *ACS Appl. Mater. Interfaces*, 2018, **10**, 8630-8639.

75 Y. Wang, J. Lv, L. Zhu and Y. Ma, *Phys. Rev. B*, 2010, **82**, 094116.

76 X. Wu, J. Dai, Y. Zhao, Z. Zhuo, J. Yang and X. C. Zeng, *ACS Nano*, 2012, **6**, 7443-7453.

77 L. M. Yang, V. Bačić, I. A. Popov, A. I. Boldyrev, T. Heine, T. Frauenheim and E. Ganz, *J. Am. Chem. Soc.*, 2015, **137**, 2757-2762.

78 C. Zhu, H. Lv, X. Qu, M. Zhang, J. Wang, S. Wen, Q. Li, Y. Geng, Z. Su and X. Wu, *J. Mater. Chem. C*, 2019, **7**, 6406-6413.

79 G. Kresse and J. Hafner, J. *Phys. Rev. B*, 1993, **47**, 558.

80 J. P. Perdew, K. Burke and M. Ernzerhof, *Phys. Rev. Lett.*, 1996, **77**, 3865.

81 S. Grimme, *J. Chem. Chem.*, 2004, **25**, 1463-1473.

82 P. E. Blöchl, *Phys. Rev. B*, 1994, **50**, 17953.

83 G. Kresse, *Phys. Rev. B*, 1999, **59**, 1758.

84 J. Heyd, G. E. Scuseria and M. Ernzerhof, *J. Chem. Phys.*, 2003, **118**, 8207-8215.

85 A. Togo, F. Oba and I. Tanaka, *Phys. Rev. B*, 2008, **78**, 134106.

86 G. J. Martyna, M. L. Klein and M. Tuckerman, *J. Chem. Phys.*, 1992, **97**, 2635-2643.

87 G. Mills and H. Jónsson, *Phys. Rev. Lett.*, 1994, **72**, 1124.

88 M. Hanfland, I. Loa and K. Syassen, *Phys. Rev. B*, 2002, 65, 184109.

89 A. Savin, R. Nesper, S. Wengert and T. F. Fässler, *Angew. Chem. Int. Ed.*, 1997, **36**, 1808-1832.

90 H. Liu, A. T. Neal, Z. Zhu, Z. Luo, X. Xu, D. Tománek and P. D. Ye, *ACS nano*, 2014, **8**, 4033-4041.

91 Q. Peng, X. Wen, S. De, *RSC Adv.*, 2013, **3**, 13772.

92 Y. Cai, G. Zhang, Y. W. Zhang, *J. Am. Chem. Soc.*, 2014,**136**, 6269–6275.

93 L. Yang, V. Bačić, I. A. Popov, A. I. Boldyrev, T. Heine, T. Frauenheim, E. Ganz, *J. Am. Chem. Soc.*, 2015, **137**, 2757-2762.

94 R. W. G. Wyckoff, Crystal Structures, 2nd ed.; Interscience Publishers: New York, 1963, Vol. 1, pp:7.

95 H. Jiang, Z. Lu, M. Wu, F. Ciucci, T. Zhao, *Nano Energy*, 2016, **23**, 97-104.

96 P. Liang, Y. Cao, B. Tai, L. Zhang, H. Shu, F. Li, D. Chao and X. Du, *J. Alloys Compd.*, 2017, **704**, 152-159.

97 Z. Zhao, T. Yu, S. Zhang, H. Xu, G. Yang, Y. Liu, *J. Mater. Chem. A*, 2019, **7**, 405-411.

98 Y. Ma, M. Eremets, A. R. Oganov, Y. Xie, I. Trojan, S. Medvedev, A. O. Lyakhov,

M. Valle and V. Prakapenka, *Nature*, 2009, **458**, 182.

99 M. S. Miao and R. Hoffmann, *J. Am. Chem. Soc.*, 2015, **137**, 3631-3637.

100 X. Zhang, Z. Yu, S. S. Wang, S. Guan, H. Y. Yang, Y. Tao, S. A. Yang, *J. Mater. Chem. A,* 2016, 4, 15224-15231.

TOC Graphic

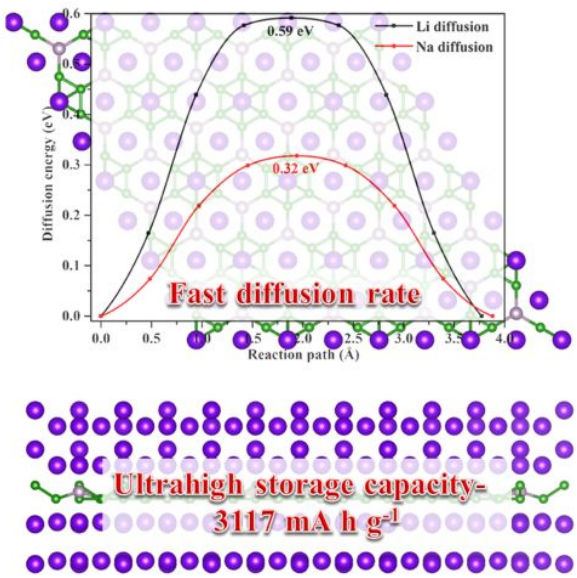

We proposed that porous 2D materials with entirely planar structure and proper pore sizes are highly promising ultrahigh storage capacity anode materials for LIBs and SIBs. Following these guidelines, by means of DFT computations, we identified the B_7P_2 monolayer, which has a capacity of 3117 mA h g^{-1}, as an excellent candidate for

ultrahigh capacity LIB/SIB anode materials, especially its capacity is among the highest for 2D SIB anodes.